Chinese Journal of Natural Medicines

Targeting TLR4 and regulating the Keap1/Nrf2 pathway with andrographolide to suppress inflammation and ferroptosis in LPS-induced acute lung injury

Yichen LI, Liting HUANG, Jilang LI, Siyuan LI, Jianzhen LV, Guoyue ZHONG, Ming GAO, Shilin YANG, Shan HAN, Wenhui HAO

Citation: Yichen LI, Liting HUANG, Jilang LI, Siyuan LI, Jianzhen LV, Guoyue ZHONG, Ming GAO, Shilin YANG, Shan HAN, Wenhui HAO, Targeting TLR4 and regulating the Keap1/Nrf2 pathway with andrographolide to suppress inflammation and ferroptosis in LPS-induced acute lung injury, Chinese Journal of Natural Medicines, 2024, 22(10), 914-928. doi: 10.1016/S1875-5364(24)60727-2.

View online: https://doi.org/10.1016/S1875-5364(24)60727-2

Wechat

Available online at www.sciencedirect.com
ScienceDirect
Chinese Journal of Natural Medicines 2024, **22**(10): 914-928
doi: 10.1016/S1875-5364(24)60727-2
Chinese Journal of Natural Medicines

•Original article•

Targeting TLR4 and regulating the Keap1/Nrf2 pathway with andrographolide to suppress inflammation and ferroptosis in LPS-induced acute lung injury

LI Yichen[1Δ], HUANG Liting[2Δ], LI Jilang[2], LI Siyuan[2], LV Jianzhen[2], ZHONG Guoyue[3], GAO Ming[1], YANG Shilin[2], HAN Shan[2, 3*], HAO Wenhui[4*]

[1] *Life Sciences Institute, Guangxi Medical University, Nanning 530021, China, ;*
[2] *College of Pharmacy, Guangxi University of Chinese Medicine, Nanning 530000, China;*
[3] *National Pharmaceutical Engineering Center for Solid Preparation in Chinese Herbal. Medicine, Jiangxi University of Traditional Chinese Medicine, Nanchang 330006, China ;*
[4] *Xinjiang Key Laboratory of Molecular Biology for Endemic Diseases, Department of Biochemistry and Molecular Biology, School of Basic Medical Sciences, Xinjiang Medical University, Urumqi 830017, China*

Available online 20 Oct., 2024

[ABSTRACT] Acute lung injury (ALI) is a severe inflammatory condition with a high mortality rate, often precipitated by sepsis. The pathophysiology of ALI involves complex mechanisms, including inflammation, oxidative stress, and ferroptosis, a novel form of regulated cell death. This study explores the therapeutic potential of andrographolide (AG), a bioactive compound derived from *Andrographis*, in mitigating Lipopolysaccharide (LPS)-induced inflammation and ferroptosis. Our research employed *in vitro* experiments with RAW264.7 macrophage cells and *in vivo* studies using a murine model of LPS-induced ALI. The results indicate that AG significantly suppresses the production of pro-inflammatory cytokines and inhibits ferroptosis in LPS-stimulated RAW264.7 cells. *In vivo*, AG treatment markedly reduces lung edema, decreases inflammatory cell infiltration, and mitigates ferroptosis in lung tissues of LPS-induced ALI mice. These protective effects are mediated *via* the modulation of the Toll-like receptor 4 (TLR4)/Kelch-like ECH-associated protein 1(Keap1)/Nuclear factor erythroid 2-related factor 2 (Nrf2) signaling pathway. Molecular docking simulations identified the binding sites of AG on the TLR4 protein (Kd value: −33.5 kcal·mol^{-1}), and these interactions were further corroborated by Cellular Thermal Shift Assay (CETSA) and SPR assays. Collectively, our findings demonstrate that AG exerts potent anti-inflammatory and anti-ferroptosis effects in LPS-induced ALI by targeting TLR4 and modulating the Keap1/Nrf2 pathway. This study underscores AG's potential as a therapeutic agent for ALI and provides new insights into its underlying mechanisms of action.

[KEY WORDS] Andrographolide; Acute lung injury; Ferroptosis; Toll-like receptor 4; Kelch-like ECH-associated protein 1/Nuclear factor erythroid 2-related factor 2

[CLC Number] R965 **[Document code]** A **[Article ID]** 2095-6975(2024)10-0914-15

Introduction

Sepsis, a potentially life-threatening condition, remains a leading cause of mortality in hospitals. Despite advanced treatment strategies, the damage, shock, and multiple organ dysfunction caused by sepsis are major contributors to patient deaths [1]. Sepsis is a primary risk factor for the frequent occurrence of acute lung injury (ALI) [2, 3]. However, the underlying mechanisms and causes of sepsis-induced ALI are not fully understood. Macrophages, essential immune cells in the lung, are particularly vulnerable during sepsis-induced ALI [4]. During sepsis, macrophages recruited and activated by lipopolysaccharides (LPS) release pro-inflammatory cytokines, leading to neutrophil (NEU) infiltration, exacerbated inflammation, endothelial barrier damage, impaired pulmonary microcirculation, and worsening lung injury [5].

Ferroptosis, a distinct form of cell death, is characterized

[Received on] 09-Oct.-2023
[Research funding] This work was supported by China-ASEAN International Innovative Center for Health Industry of Traditional Chinese Medicine (No. AD20297142) and Guangxi Collaborative Innovation Center for Scientific Achievements Transformation and Applicationon Traditional Chinese Medicine (No. 05020058).
[*Corresponding author] E-mails: hanshan201807@163.com (HAN Shan); haowenhui@xjmu.edu.cn (HAO Wenhui)
[Δ]These authors contributed equally to this work.
These authors have no conflict of interest to declare.

by the accumulation of lipid peroxides and intracellular iron, resulting in mitochondrial shrinkage and altered expression of genes such as glutathione (GSH) peroxidase 4 (GPX4) and the cystine/glutamate transporter (SLC7A11) [6, 7]. Ferroptosis has been implicated in various diseases, including cancer [8], neurological disorders [9], ischemia/reperfusion injury [10], and lung injury [11]. Recent research highlights the crucial role of ferroptosis in the development of multi-organ damage induced by sepsis. Inhibition of ferroptosis significantly reduces the severity of organ damage, including cardiac injury [12], ALI [4], and renal injury [13]. Studies have shown that LPS treatment decreases ferroptosis markers such as SLC7A11, GPX4, GSH, and malondialdehyde (MDA) in ALI models while increasing lipid peroxide and intracellular iron levels, leading to lung injury. Conversely, the use of the ferroptosis inhibitor ferrostatin substantially improves cell viability, reduces lipid peroxide and intracellular iron levels, and mitigates lung injury [14]. Therefore, targeting ferroptosis presents a promising strategy for the treatment of LPS-induced lung injury.

The development of ALI critically involves toll-like receptor 4 (TLR4) and nuclear factor erythroid 2-related factor 2 (Nrf2) [15, 16]. Activation of TLR4 initiates inflammatory signaling pathways, leading to increased inflammation and organ damage [17]. In contrast, Nrf2 serves as a key regulator of antioxidant defense, maintaining cellular redox homeostasis and preventing oxidative damage [18, 19]. Research indicates that TLR4 recognizes LPS, triggering a series of signaling pathways involving nuclear factor-kappa B (NF-κB), which results in the release of pro-inflammatory cytokines and reactive oxygen species (ROS), thereby intensifying oxidative stress. Nrf2 plays a crucial role in preventing lipid peroxidation and inhibiting ferroptosis by regulating the expression of signaling proteins and enzymes, such as SLC7A11 and GPX4, by activating downstream genes [20].

Andrographis (Burm. F) Nees contains several bioactive compounds with anti-inflammatory properties that modulate immune function, interact with platelet-activating factors, scavenge oxygen free radicals, inhibit various pro-inflammatory cytokines, and exhibit potent anti-inflammatory effects [21]. Andrographolide, which constitutes 70% of *Andrographis* extract, exhibits a range of biological activities including anti-inflammatory [22], anticancer [23], antiviral [24], antibacterial [25], and antioxidant effects [26]. This study demonstrates that andrographolide (AG) effectively inhibits inflammation and ferroptosis in LPS-induced ALI by targeting TLR4 and modulating the Kelch-like ECH-associated protein 1(Keap1)/Nrf2 pathway.

Materials and Methods

Reagents

Andrographolide (AG) was obtained from Chengdu Biopurify Phytochemicals Ltd. (Chengdu, China). Its purity was 98%, and its CAS number is #5508-58-7. LPS from *Escherichia coli* O111:B5, MTT, and 2',7'-dichlorodihydrofluorescein diacetate ($DCFH_2$-DA) were purchased from Sigma-Aldrich (St. Louis, MO, USA). C11 BODIPY 581/591 (GC40165) was obtained from GlpBio (Montclair, USA). FerroOrange (F374) was obtained from Dojindo (Kumamoto, Japan). ML385 (HY100523) was purchased from MedChemExpress (Princeton, USA). MDA and GSH kits were purchased from Nanjing Jiancheng Bioengineering (Nanjing, China). The Nuclear and Cytoplasmic Protein Extraction Kit was obtained from Beyotime (Shanghai, China). Antibodies against COX-2 (#4842), iNOS (#2977S), TLR4 (#14358), Keap1 (#4678), Nrf2 (#12721), HO-1 (#70081), PARP (#9532), GAPDH (#5174), and Anti-rabbit IgG, HRP-linked Antibody (#7074) were acquired from Cell Signaling (Beverly, MA, USA). NQO1 (ab80588) was purchased from Abcam (Cambridge, MA, USA). SLC7A11 (DF12509) and GPX4 (AF6701) were obtained from Affinity Biosciences (Cincinnati, OH, USA).

Cell culture

The RAW264.7 cell line was sourced from BeiNa Culture, Henan Province, China. The cells were cultured in DMEM medium supplemented with 10% fetal bovine serum (FBS), 100 $U \cdot mL^{-1}$ penicillin, and 100 $\mu g \cdot mL^{-1}$ streptomycin. The cultures were maintained in a humidified incubator at 37 °C with 5% CO_2.

MTT assay

RAW264.7 cells were seeded at a density of 1×10^4 cells per well in 96-well culture plates. The cells were pre-treated with AG at concentrations of 1.25, 2.5, and 5 $\mu mol \cdot L^{-1}$ for 2 h. Following this pre-treatment, the cells were exposed to LPS at a concentration of 100 $\mu g \cdot mL^{-1}$ for 48 h. Cell viability was then assessed using the MTT assay. The cells were incubated with MTT reagent at 5 $mg \cdot mL^{-1}$ for 3 h. After incubation, the culture medium was removed, and the formazan crystals formed were dissolved in 100 μL of DMSO per well. The absorbance was measured at 570 nm using a microplate reader.

Analysis of intracellular ROS levels

Cells were pre-treated with AG for 2 h, followed by exposure to LPS for 48 h. After this, the cells were incubated with 1 $\mu mol \cdot L^{-1}$ $DCFH_2$-DA diacetate in the dark at room temperature for 30 min. Following incubation, the cells were washed three times with PBS. Intracellular ROS levels were then visualized using a fluorescence microscope. Additionally, ROS levels were quantified using a flow cytometer (Becton-Dickinson, Franklin Lakes, NJ, USA).

Analysis of lipid peroxidation and Fe^{2+}

RAW264.7 cells were washed three times with PBS before incubation with 1 $\mu mol \cdot L^{-1}$ C11 BODIPY 581/591 and Ferro Orange to measure lipid peroxide and Fe^{2+} levels, respectively. After 30 minutes of incubation at room temperature in the dark, the cells were washed three additional times with PBS. Lipid peroxide levels were visualized using a confocal microscope (Leica, Wetzlar, Germany). For quantitative analysis, cells were harvested, and lipid peroxide and Fe^{2+} llevels were measured using flow cytometry (Becton-Dickinson, Franklin Lakes, NJ, USA).

Measurement of GSH, MDA, and Fe^{2+}

Total GSH, MDA, and Fe^{2+} levels in cell or tissue lysates were measured using specific colorimetric assay kits for GSH, MDA, and ferrous iron. These assays were performed according to the manufacturer's protocols.

Immunofluorescence

RAW264.7 cells were pre-treated with 5 μmol·L^{-1} AG for 2 h, followed by treatment with 100 μg·mL^{-1} LPS for 48 h. The cells were then washed three times with PBS and fixed with 4% paraformaldehyde (PFA) for 30 min at room temperature. Cells were permeabilized with 0.5% Triton X-100 for 15 min and blocked with 5% bovine serum albumin (BSA) for 30 min. The samples were incubated overnight at 4°C with primary antibodies against GPX4 or Nrf2. The next day, cells were incubated for 2 h at room temperature with Coralite 488 goat anti-rabbit IgG (SA00013-2, Proteintech, China) or Coralite 594 goat anti-rabbit IgG (SA0001d-4, Proteintech, China). Finally, the cells were stained with Hoechst 33342 for 10 min, and immunofluorescent images were captured using a confocal laser scanning microscope (Leica TCS SP8, Solms, Germany).

Real-time quantitative polymerase chain reaction (RT-PCR) analysis

RAW 264.7 cells were pre-treated with AG at concentrations of 1.25, 2.5, and 5 μmol·L^{-1} for 2 h, followed by treatment with 100 μg·mL^{-1} LPS. Total RNA was extracted and used for qRT-PCR analysis with 1 μg of RNA. SYBR Green was utilized for PCR amplification. Specific oligonucleotide primers were used to target *TNF-α*, *IL-6*, *Nrf2*, *Keap-1*, *HO-1*, *NQO-1*, *GPX4*, *SLC7A11*, and *GAPDH* (Table 1).

Table 1 Primer sequences

Target	Forward primer	Reverse primer	Gene bank number	Size of primers/bp
TNF-α	CTACTGAACTTCGGGGTGAT	TTGGTGGTTTGTGAGTGTGA	21926 Mouse	105
IL-6	TTGGGACTGATGCTGGTGAC	CTTTTCTCATTTCCACGATTTC	16193 Mouse	160
Nrf2	CAGCCATGACTGATTTAAGCAG	CAGCTGCTTGTTTTCGGTATTA	18024 Mouse	107
Keap1	TGCTCAACCGCTTGCTGTATGC	TCATCCGCCACTCATTCCTCTCTG	50868 Mouse	99
HO-1	GAAGCAGCTGCAGAAGAGATTT	CATAAACTCACTGAACCGCTTC	18155 Mouse	91
NQO-1	AGGAGACCCCACTCTATTTTGC	AATGGACTTGCCCAGGTGAT	18104 Mouse	143
GPX4	ATAAGAACGGCTGCGTGGTGAAG	TAGAGATAGCACGGCAGGTCCTTC	625249 Mouse	82
SLC7A11	CTATTTTACCACCATCAGTGCG	ATCGGGACTGCTAATGAGAATT	26570 Mouse	102
GAPDH	GGTTGTCTCCTGCGACTTCA	TGGTCCAGGGTTTCTTACTCC	100042025 Mouse	183

Western blotting assay

RAW264.7 cells were pre-treated with AG at concentrations of 1.25, 2.5, and 5 μmol·L^{-1} for 2 h before stimulation with 100 μg·mL^{-1} LPS. The cells were lysed using RIPA buffer, and the lysates were mixed with Sodium dodecyl-sulfate polyacrylamide gel electrophoresis (SDS-PAGE) reducing sample buffer. Denatured proteins were separated on SDS-PAGE gels (8%, 10%, or 12%) and transferred onto PVDF membranes (Millipore, Billerica, MA, USA). To block non-specific binding, the membranes were incubated with 5% non-fat milk for 2 h. They were then exposed to primary antibodies at a 1∶1000 dilution overnight at 4°C, followed by incubation with secondary antibodies at a 1∶5000 dilution for 2 h at room temperature. Protein bands were detected using theSuperSignalWestFemtoMaximumSensitivitySubstrate(Pierce Biotechnology, USA) and visualized with a ChemiDoc MP Imaging System (Bio-Rad, Hercules, CA, USA).

Cellular Thermal Shift Assay (CESTA) [27]

HEK293T cells were lysed using Radio-Immunoprecipitation Assay (RIPA) buffer containing 1% phenylmethylsulfonyl fluoride (PMSF) and 1% protease inhibitor cocktail to disrupt cell membranes. The cell lysates were then incubated on ice for 30 min with either DMSO (control) or 5 μmol·L^{-1} AG. Following incubation, samples were centrifuged at 15 000 r·min^{-1} for 30 min at 4 °C. The supernatants were divided into six aliquots and subjected to different temperatures (36, 40, 44, 48, 52, and 56 °C) for 3 min each. The samples were then cooled to room temperature for 30 s and analyzed using Western blotting analysis.

Molecular docking

The two-dimensional (2D) structure of AG was sourced from the PubChem database in sdf format. To convert this into a three-dimensional (3D) structure, energy minimization was performed using ChemBio3D, and the structure was saved in mol2 format. The 3D structure of TLR4 (PDB code: 3FXI) was retrieved from the RCSB PDB database. Using PyMol software, water molecules and the original ligand were removed from the TLR4 structure. The TLR4 protein was designated as the receptor, and the AG molecule as the ligand. Active sites for molecular docking were identified using the coordinates of the ligands in the TLR4 complex. Molecular docking was performed with AutoDock Vina. The docking results were then analyzed and visualized using PyMol.

Surface plasmon resonance (SPR) analysis

SPR analysis was performed using a Biacore X100 system equipped with a CM5 sensor chip. Recombinant human TLR4 was immobilized on the CM5 chip *via* an amine-coup-

ling protocol. AG was prepared in seven different concentrations (1.5625, 3.125, 6.25, 12.5, 25, 50, and 100 nmol·L^{-1}) in HBS-EP buffer. These concentrations were introduced into the flow system at a rate of 20 μL·min^{-1}. The association phase was recorded for 120 s, followed by a 300-second dissociation phase. Binding kinetics were analyzed using Biaevaluation 2.0 software.

Animal treatment

Ethical approval for this study was obtained from the Animal Policy and Welfare Committee of Guangxi University of Chinese Medicine (Approval Document No. SYXK-GUI-2019-0001). All procedures conformed to the guidelines for the care and use of laboratory animals. Male BALB/c mice (6−8 weeks old, weighing 18−22 g) were procured from Vital River Laboratory (Guangdong, China) and housed under specific pathogen-free (SPF) conditions at 25 °C with 50% humidity, with unrestricted access to food and water. To induce ALI, the mice were randomly assigned to the following groups: control group, LPS group (intratracheal administration of 10 mg·kg^{-1} LPS), AG treatment groups (intraperitoneal administration of AG at 10 and 40 mg·kg^{-1}), and a positive control group (intraperitoneal administration of dexamethasone (DEX) at 5 mg·kg^{-1}). Each group contained six mice. AG was administered at 0, 6, and 12 h post-LPS administration, while DEX was administered only at 0 h. After 24 h of LPS treatment, lung tissue samples were collected for analysis. Levels of MDA and GSH in lung homogenates were measured using commercial assay kits. A portion of the lung tissue was fixed in 4% paraformaldehyde, embedded in paraffin, and processed for histological analysis. The remaining lung tissue was used for protein analysis *via* Western blotting analysis. Additionally, blood samples were collected to measure lymphocyte (Lym) and NEU levels.

Hematoxylin and Eosin (HE) staining and single immunofluorescence

Lung tissue samples were fixed using a 4% PFA solution, then segmented and stained with HE. Tissue slides were then prepared, enabling the examination of pathological changes under light microscopy. The tissue samples were frozen, sectioned, and then gradually brought back to room temperature. The sections were then treated with a PBS solution containing C11 BODIPY 581/591, followed by a 30 mins incubation period. Finally, the production of Lip-ROS in the mouse lung tissue samples was assessed using fluorescence microscopy.

Statistical analysis

Data were derived from three independent experiments and are presented as mean ± standard deviation. Statistical analyses were conducted using GraphPad Prism 6.0 software (GraphPad Software, San Diego, CA, USA). One-way ANOVA, followed by Dunnett's test for multiple comparisons, was utilized to evaluate the data. Statistical significance was determined at thresholds of $^{*}P < 0.05$, $^{**}P < 0.01$, and $^{***}P < 0.001$.

Results

AG reverses LPS-induced cell death and exerts anti-inflammatory activity

The cytotoxic effects of AG (Fig. 1A) on RAW 264.7 cells were assessed. AG exhibited negligible cytotoxicity at concentrations of 1.25, 2.5, or 5 μmol·L^{-1} (Fig. 1B). Treatment with LPS for 48 h significantly decreased cell viability, while AG at these concentrations enhanced cell survival (Figs. 1C and 1D). LPS is known to induce the production of inflammatory cytokines Interleukin 6 (IL-6) and Tumor necrosis factor alpha (TNF-α) in RAW 264.7 cells. Stimulation with LPS resulted in elevated mRNA levels of *IL-6* and *TNF-α*, which were significantly reduced by AG at 5 μmol·L^{-1} (Fig. 1E). Furthermore, AG inhibited the LPS-induced upregulation of COX-2 and iNOS, both of which are key inflammatory markers commonly assessed in various inflammatory models (Fig. 1F). Pre-treatment with AG also significantly reduced the protein expression and mRNA levels of COX-2 and iNOS induced by LPS (Figs. 1G and 1H). In summary, AG effectively reverses LPS-induced cell death and suppresses inflammatory responses by reducing the levels of IL-6, TNF-α, iNOS, and COX-2.

AG inhibits ferroptosis in LPS-induced RAW 264.7 cells

Ferroptosis, a recently identified form of regulated cell death, is marked by excessive iron accumulation and lipid peroxidation [28]. Different cell types exhibit varying sensitivity to ferroptosis. In RAW 264.7 cells treated with LPS, there was a significant increase in lipid peroxide production (measured as MDA) (Fig. 2A) and a decrease in GSH levels (Fig. 2B), both indicative of ferroptosis. Treatment with AG mitigated these effects, showing a protective impact on these markers (Figs. 2A and 2B). Lipid peroxidation and Fe^{2+} accumulation are critical features of ferroptosis. LPS-treated RAW 264.7 cells exhibited a notable increase in lipid peroxidation, as evidenced by heightened green fluorescence. AG treatment significantly reduced this fluorescence intensity (Fig. 2D). Consistent with these immunofluorescence findings, LPS exposure led to significant lipid ROS accumulation, indicated by increased green fluorescence in the cytoplasm. AG treatment partially reversed this accumulation, as confirmed by flow cytometry (Figs. 2C and 2E). Flow cytometry analysis also revealed that LPS treatment elevated Fe^{2+} levels in RAW 264.7 cells. However, AG pre-treatment partially mitigated this increase (Supplementary Figs. 1A and 1B). Additionally, the levels of GPX4 and SLC7A11, crucial proteins associated with lipid peroxidation, were assessed. Western blotting analysis showed that LPS administration decreased the protein levels of GPX4 and SLC7A11, whereas AG treatment increased their expression in the presence of LPS (Fig. 2G). AG pre-treatment also significantly counteracted the LPS-induced downregulation of GPX4 and SLC7A11 mRNA levels (Fig. 2F). In Fig. 2H, immunofluorescence assays revealed a substantial reduction in GPX4 expression in RAW 264.7 cells exposed to LPS, as indicated by

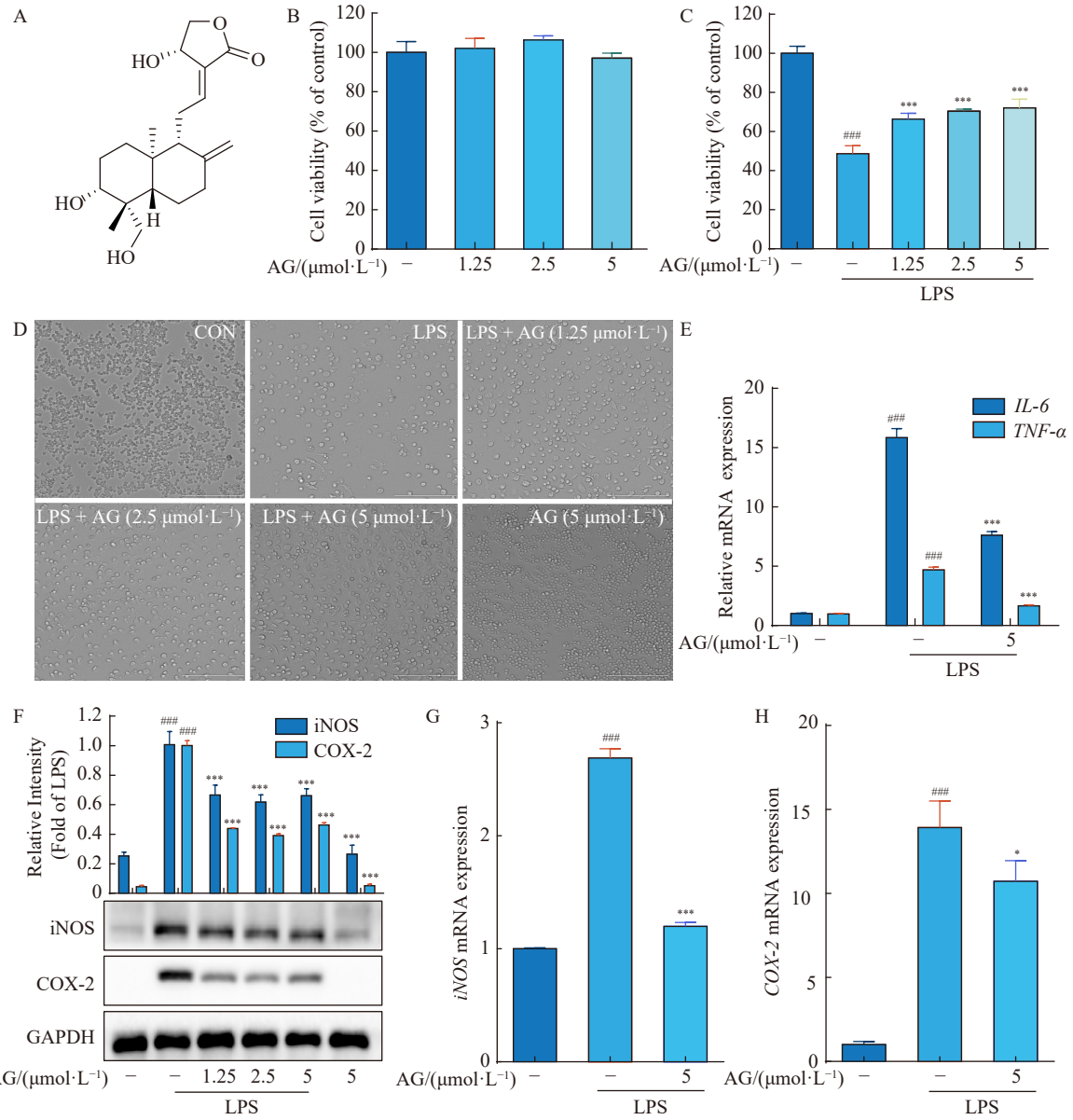

Fig. 1 AG reverses LPS-induced cell death and exerts anti-inflammatory activity. (A) Chemical structure of AG is depicted. (B) The impact of AG on cell viability in RAW 264.7 cells was assessed. (C) RAW264.7 cells were exposed to AG for 2 h, followed by a 48-h treatment with LPS. Cell cytotoxicity was determined using the MTT assay. (D) After subjecting RAW 264.7 cells to 2 h of AG treatment followed by 48 h of LPS treatment, significant morphological changes were observed (scale bar = 100 μm). (E) RT-qPCR was employed to quantify the mRNA levels of *IL-6* and *TNF-α*. (F) iNOS and COX-2 expressions were detected through immunoblotting analysis. (G and H) The levels of *iNOS* and *COX-2* mRNA were quantified. Data were shown as mean ± SD (n = 3). Statistical analysis revealed significant differences: $^{\#\#\#}P < 0.001$ *vs* control; $^{***}P < 0.001$, $^{*}P < 0.05$ *vs* LPS group.

diminished red fluorescence in both the cytoplasm and nucleus. However, AG treatment markedly increased GPX4 fluorescence. In summary, these results indicate that LPS induces ferroptosis in RAW 264.7 cells, and pre-treatment with AG can partially inhibit this process.

AG inhibits ferroptosis by regulating the Keap1/Nrf2 signaling pathway in LPS-induced RAW 264.7 cells

Nrf2, a crucial transcription factor in oxidative stress responses, activates various target genes that regulate ferroptosis through the modulation of GSH and lipid metabolism [29]. Under normal conditions, Nrf2 is sequestered in the cytoplasm by Keap1. During oxidative stress, Keap1 is degraded, releasing Nrf2, which then translocates to the nucleus. Once in the nucleus, Nrf2 activates the expression of antioxidant genes such as HO-1 and NQO-1 [18]. In this study, treatment with AG increased the expression of Nrf2, HO-1, and NQO-1 while decreasing the expression of Keap1 in LPS-induced RAW 264.7 cells (Figs. 3A and 3B). Furthermore, AG treatment downregulated Keap1 mRNA levels and upregulated the mRNA levels of *Nrf2*, *HO-1*, and *NQO1* (Fig. 3C). The findings depicted in Fig. 3D demonstrate that AG treatment led to a reduction in cytoplasmic Nrf2 and an increase in nuc-

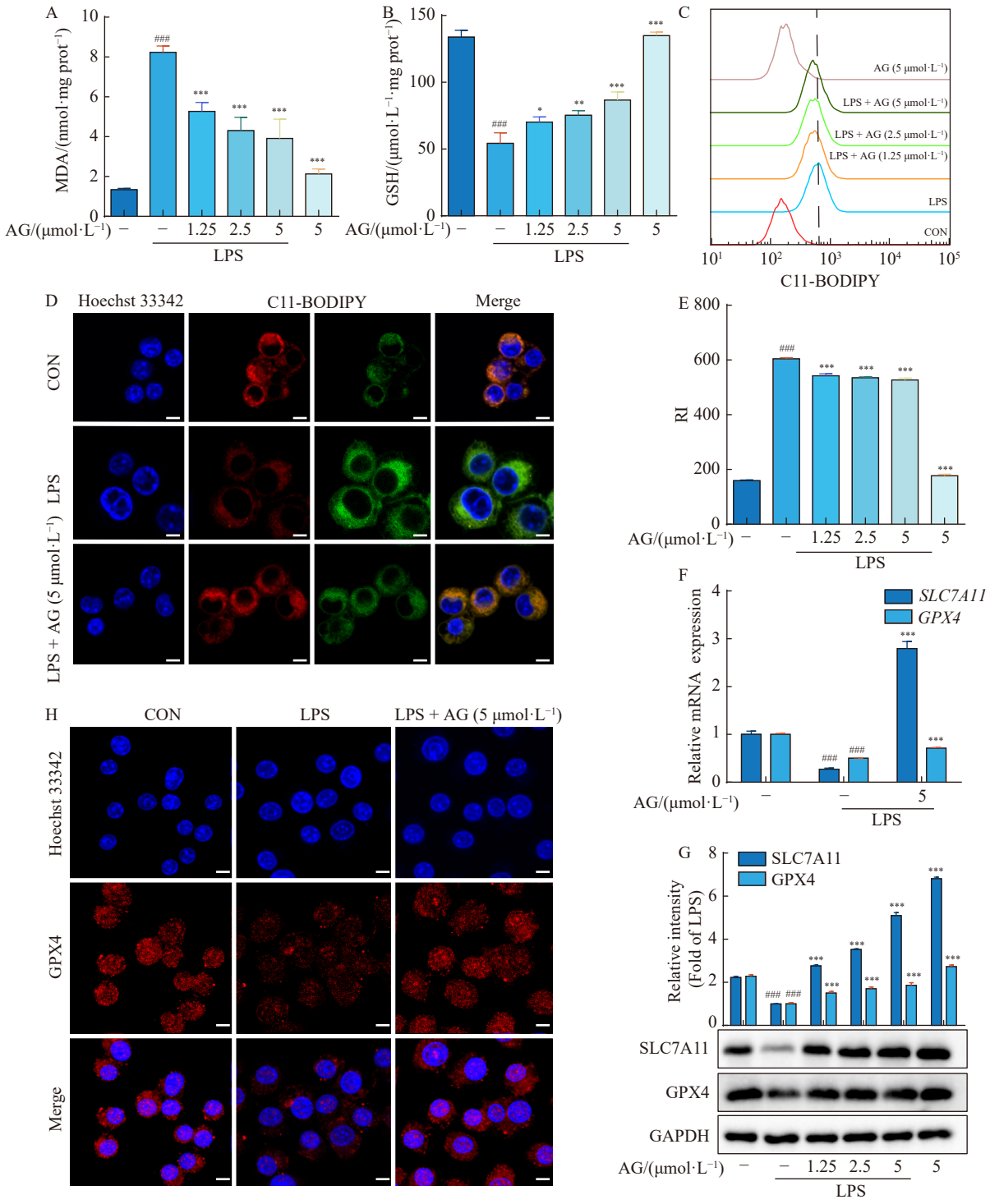

Fig. 2 AG inhibits ferroptosis in LPS-induced RAW 264.7 cells. (A, B) The kits were utilized to determine the levels of MDA (A) and GSH (B). (C) To analyze lip-ROS generation in RAW 264.7 cells exposed to the respective stimuli, BODIPY 581/591 was employed as a probe, and flow cytometry was utilized for measurement. (E) We conducted a measurement of lipid ROS levels. (D) To visualize lipid ROS, we employed confocal imaging in RAW 264.7 cells that were stimulated with LPS and stained the cell nucleus using Hoechst 33342 (Scale bar = 25 μm). (F) The mRNA expression levels of *SLC7A11* and *GPX4* were determined using RT-qPCR. (G) We evaluated the levels of SLC7A11 and GPX4 expression through immunoblotting analysis. (H) Immunofluorescence analysis was performed to determine the expression levels of GPX4, and the cell nucleus was stained by Hoechst 33342 (Scale bar = 25 μm). Data were shown as mean ± SD (n =3). Statistical analysis revealed significant differences: $^{###}P < 0.001$ *vs* control; $^{***}P < 0.001$, $^{**}P < 0.01$, and $^{*}P < 0.05$ *vs* LPS group.

lear Nrf2, as evidenced by the observed shift of green fluorescence from the cytoplasm to the nucleus. This is evident from the observed shift of green fluorescence from the cytoplasm to the nucleus. This suggests that AG promotes Nrf2 translocation to the nucleus. Immunofluorescence analysis further confirmed that AG facilitates Nrf2 nuclear translocation (Fig. 3E). Elevated cellular ROS levels are a primary trigger and hallmark of ferroptosis [30]. LPS-treated cells showed significant ROS accumulation, which was partially reversed by AG pre-treatment, as indicated by flow cytometry analysis (Figs. 3F and 3G). Additionally, AG pre-treatment substantially reduced ROS fluorescence intensity in LPS-treated RAW 264.7 cells (Fig. 3H). To further elucidate the role of the Nrf2 pathway in AG-mediated ferroptosis inhibition, RAW 264.7 cells were treated with ML385 (1 μmol·L^{-1}), an Nrf2 inhibitor. The results indicated that AG's ability to increase GPX4 and SLC7A11 protein expression was significantly diminished when the Nrf2 pathway was inhibited, suggesting that the Keap1/Nrf2 pathway is essential for AG-mediated ferroptosis inhibition in RAW 264.7 cells (Supplementary Fig. 2).

LPS activates ferroptosis by activating TLR4

To investigate the TLR4-mediated effects of AG on ferroptosis in LPS-induced RAW 264.7 cells, a series of experiments were conducted. Initially, LPS administration significantly reduced cell viability. However, treatment with TAK-242, a TLR4 inhibitor, increased the number of viable cells following LPS exposure (Fig. 4A). LPS treatment led to elevated levels of lipid peroxides (MDA) and a reduction in GSH levels, both of which are characteristic indicators of ferroptosis (Figs. 4B and 4C). Treatment with TAK-242 reversed these changes, demonstrating a protective effect in RAW 264.7 cells (Figs. 4B and 4C). Immunofluorescence analysis using the lipid peroxidation sensor C11-BODIPY showed reduced green fluorescence intensity in the cytoplasm of cells pre-treated with TAK-242, indicating decreased lipid peroxidation (Fig. 4D). Additionally, flow cytometry analysis revealed that TAK-242 partially reversed the LPS-induced accumulation of lipid ROS (Figs. 4E and 4F). To explore the underlying mechanisms, the levels of GPX4 and SLC7A11, which are associated with lipid peroxidation, were assessed. TAK-242 treatment upregulated the levels of SLC7A11 and GPX4 in LPS-induced RAW 264.7 cells, as shown by both Western blotting and RT-qPCR analyses (Figs. 4G−4I). Furthermore, TAK-242 administration decreased Keap1 protein and mRNA levels while increasing Nrf2 protein and mRNA levels (Figs. 4G−4I). These results suggest that TLR4 functions upstream of the Keap1/Nrf2 pathway, corroborating previous research findings. In summary, our results indicate that LPS triggers ferroptosis in RAW 264.7 cells by activating TLR4 and that downregulation of TLR4 expression can partially mitigate this process.

AG inhibits LPS-induced ferroptosis by interacting with TLR4

This study aimed to investigate the inhibitory effects of AG on TLR4 levels in RAW 264.7 cells exposed to LPS. Our findings demonstrated that AG effectively suppressed TLR4 levels (Fig. 5A). To further validate the interaction between AG and TLR4, we performed a CETSA, which confirmed that AG increased the stability of the TLR4 protein across various temperatures (40, 44, 48, 52, and 56 °C) (Fig. 5B). To elucidate the kinetics and affinity between AG and TLR4, we utilized a SPR assay with the Biacore X100 system. The results revealed a strong interaction between AG and TLR4, with a dissociation constant (K_D) of 3.51 μmol·L^{-1} (Figs. 5C and 5D). Molecular docking analysis was then employed to identify the specific binding sites of AG on TLR4. The predicted binding energy of AG with TLR4 was −33.5 kcal·mol^{-1}. The analysis indicated that AG interacts with the ARG227, LEU204, GLU286, and ASN205 residues of TLR4 (Figs. 5E and 5F). In summary, these findings suggest that AG inhibits ferroptosis in LPS-induced RAW 264.7 cells by directly interacting with TLR4.

AG significantly alleviates LPS-induced ALI in vivo

We investigated the protective role of AG in a mouse model of ALI. Administering AG before LPS exposure effectively alleviated ALI symptoms, resulting in reduced pulmonary hemorrhage, interstitial edema, thickening of alveolar walls, and overall tissue damage (Fig. 6A). Additionally, AG treatment reversed the LPS-induced increase in the lung wet-to-dry weight ratio (Fig. 6B). LPS treatment significantly elevated NEU and lymphocyte counts in the blood of mice, whereas AG pre-treatment markedly reduced these cell counts (Figs. 6C and 6D). Furthermore, AG mitigated the inflammatory response in pulmonary tissues induced by LPS, as demonstrated by the reduction in mRNA levels of *IL-6* and *TNF-α* (Fig. 6G). Inflammatory markers such as iNOS and COX-2 were assessed due to their substantial alterations in various inflammatory models. AG effectively suppressed the expression of COX-2 and iNOS in the pulmonary tissues of LPS-treated mice (Figs. 7B and 7D). In summary, these findings indicate that AG has a significant protective effect against LPS-induced ALI in mice.

AG reduced LPS-induced ferroptosis in lung tissues

To investigate the role of AG in modulating ferroptosis during ALI, we evaluated key markers of lipid peroxidation, specifically MDA and GSH. LPS administration led to a significant reduction in GSH levels and an increase in MDA levels, indicating enhanced lipid peroxidation. However, AG treatment effectively reversed these changes (Figs. 6E and 7F). AG also reduced the elevated levels of tissue lipid ROS induced by LPS (Fig. 7A). The accumulation of Fe^{2+} is another hallmark of ferroptosis. Supplementary Fig. 3 shows that LPS induction resulted in elevated Fe^{2+} levels in lung tissue compared to the control group. However, AG intervention effectively reversed this LPS-induced increase in Fe^{2+} levels. The GSH-dependent antioxidant enzyme GPX4 is crucial for inhibiting ferroptosis. We assessed the expression of GPX4 and SLC7A11, both markers of ferroptosis, in lung tissues. LPS administration decreased the protein and mRNA levels of GPX4 and SLC7A11 (Figs. 7C and 7D). Notably, AG pre-

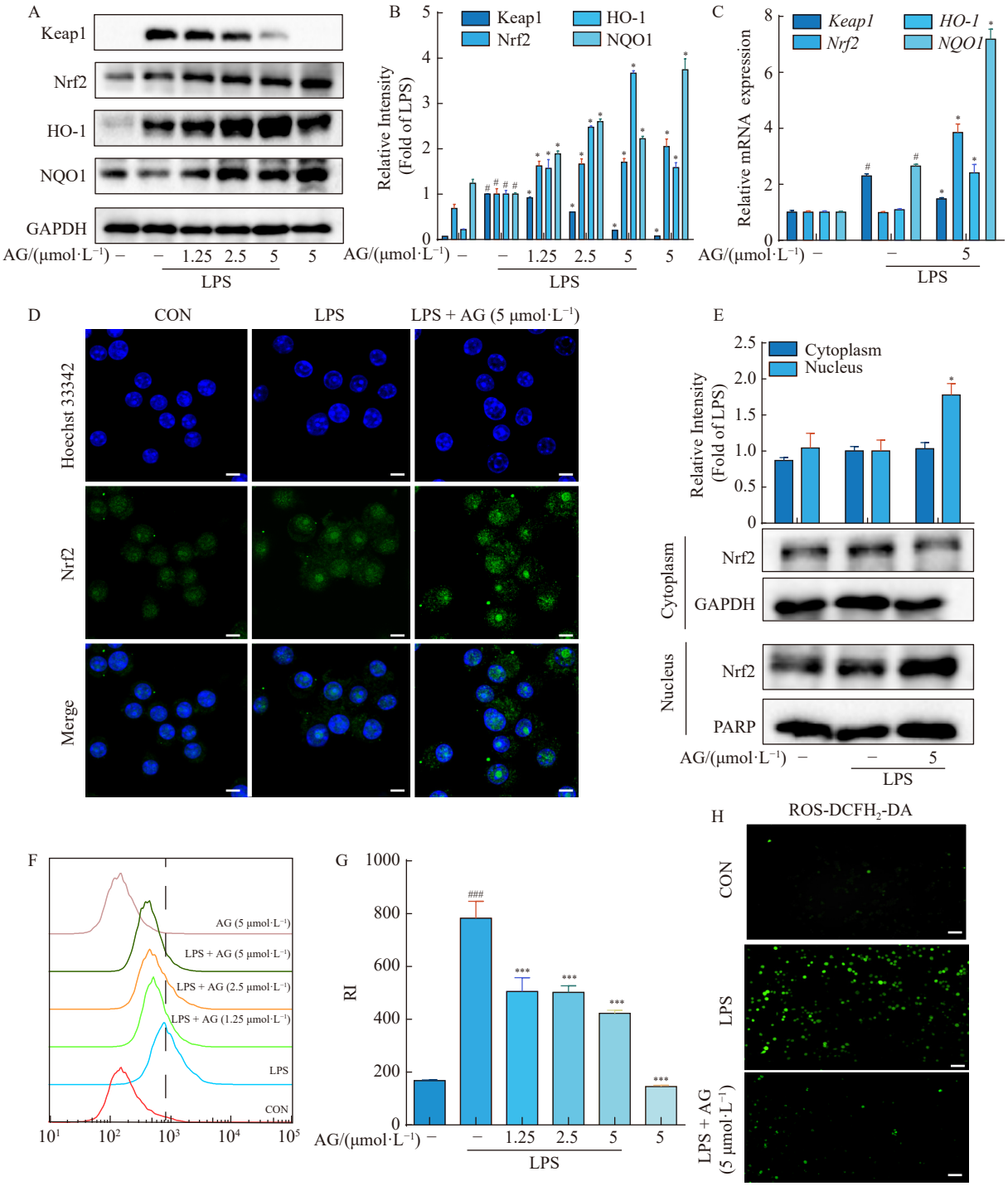

Fig. 3 AG inhibits ferroptosis by regulating the Keap1/Nrf2 signaling pathway in LPS-induced RAW 264.7 cells. (A) We conducted immunoblotting analysis to evaluate the expression levels of Keap1, Nrf2, HO-1, and NQO1. (B) Statistical analysis was carried out to compare the levels of Keap1, Nrf2, HO-1, and NQO1 among the different groups. (C) We utilized RT-qPCR to assess the expression levels of *Keap1*, *Nrf2*, *HO-1*, and *NQO1* mRNA. (D) Immunofluorescence analysis was performed to examine the translocation of Nrf2, and the cell nucleus was stained by Hoechst 33342 (Scale bar = 25 μm). (E) Western blotting assay was employed to detect the localization of Nrf2 in both the cytoplasm and nucleus. (F) Flow cytometry using $DCFH_2$-DA staining (1 μmol·L^{-1}) was employed to investigate ROS production. (G) Quantification of lipid ROS was also performed. (H) We observed the inhibitory effects of AG on the fluorescence of ROS in RAW 264.7 cells induced by LPS. The scale bar in the image is 100 μm. Data were shown as mean ± SD (n =3). Statistical analysis demonstrated significant differences: $^{###}P < 0.001$, $^{#}P < 0.05$ *vs* control group; $^{***}P < 0.001$, and $^{*}P < 0.05$ *vs* LPS group.

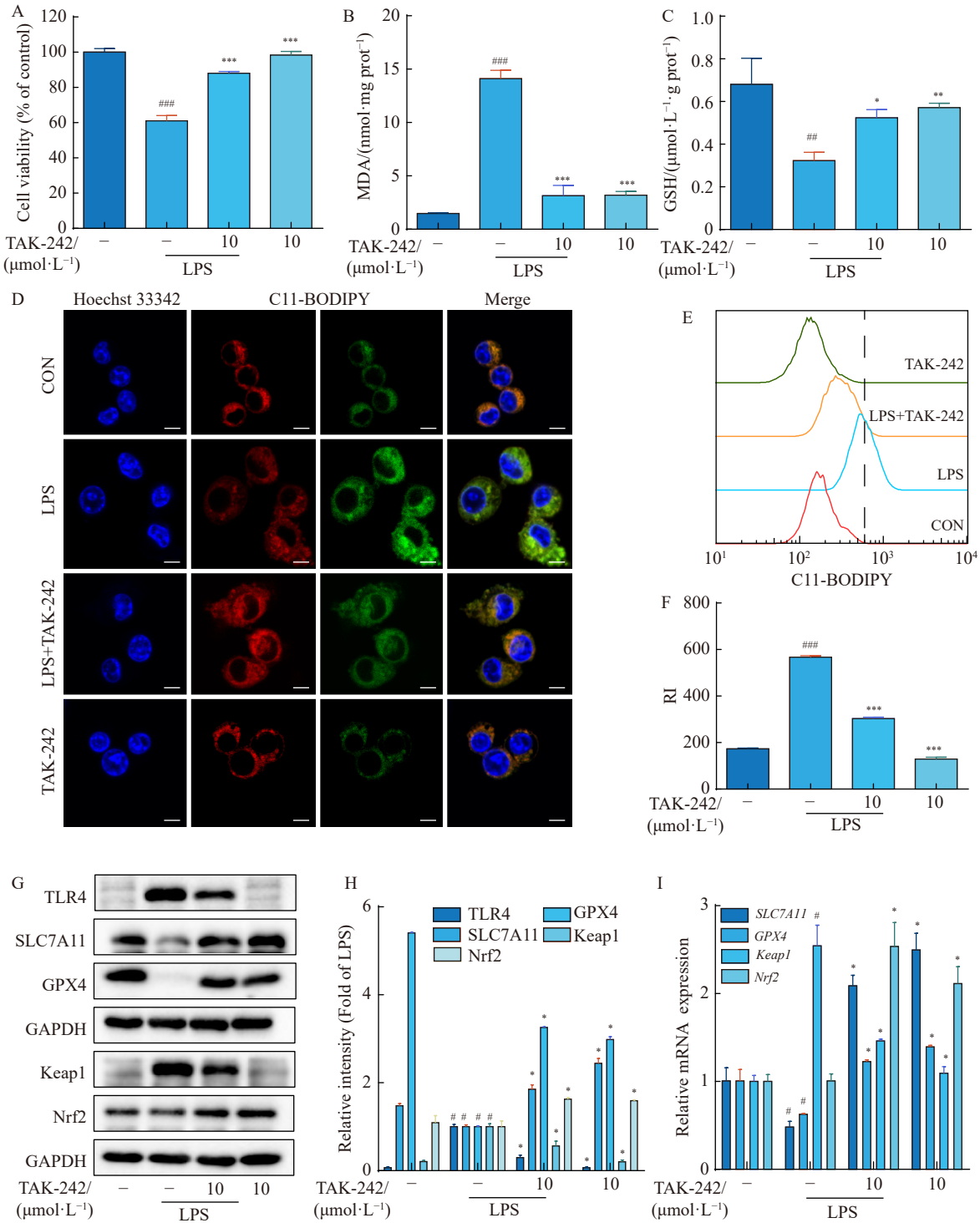

Fig. 4 LPS activates ferroptosis by activating TLR4. Prior to 48 h LPS stimulation, RAW 264.7 cells were pre-treated with TAK-242 (10 μmol·L^{-1}) for 2 h. (A) TAK-242 cytotoxicity was assessed by MTT assay. (B and C) The effects of TAK-242 on the levels of MDA (lipid peroxide) (B) and the levels of GSH (C) in LPS-induced RAW 264.7 cells were determined. (D) The effect of TAK-242 on lipid ROS levels in LPS-induced RAW 264.7 cells was evaluated by immunofluorescence (scale bar = 25μm). (E and F) The levels of lipid ROS in LPS-induced RAW 264.7 cells were measured by flow cytometry. (G and H) Effect of TAK-242 on specific protein expression in LPS-induced RAW 264.7 cells. (I) *SLC7A11*, *GPX4*, *Keap1*, and *Nrf2* mRNA levels were assessed by RT-qPCR. Data were shown as mean ± SD (n =3). Statistical analysis revealed significant differences: $^{###}P < 0.001$, $^{#}P < 0.05$ *vs* control; $^{***}P < 0.001$, $^{**}P < 0.01$, and $^{*}P < 0.05$ *vs* LPS group.

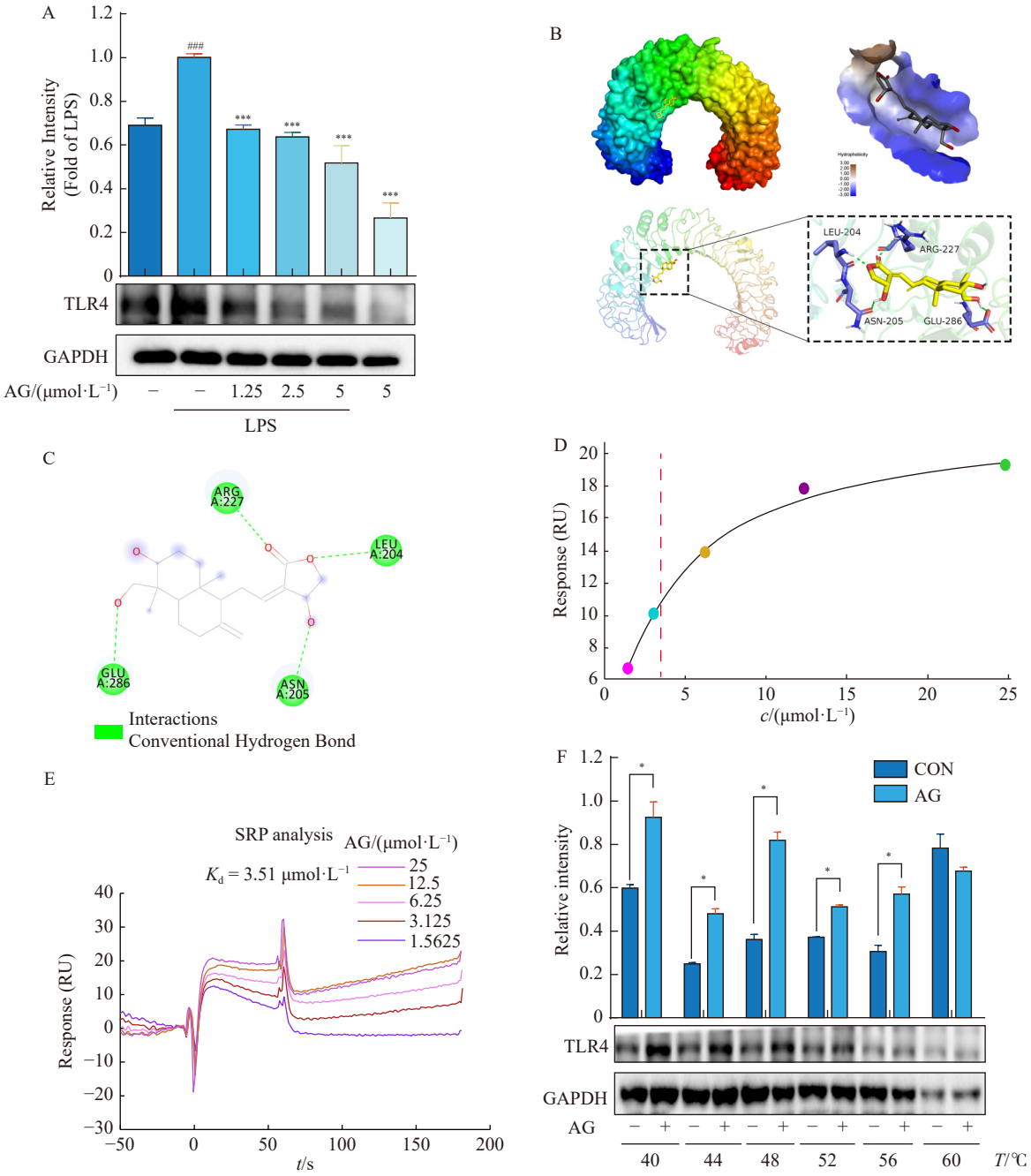

Fig. 5 AG interacting with TLR4. (A) The impact of AG on the expression of TLR4 proteins in LPS-induced RAW 264.7 cells was assessed. (B, C) Molecular docking analysis was conducted to examine the binding of AG with TLR4. (D, E) The kinetics and affinity of AG with TLR4 were determined using Biacore X100. (F) The interaction between AG and TLR4 was investigated using CETSA. Data were shown as mean ± SD (n =3). Statistical analysis revealed significant differences: $^{###}P < 0.001$ *vs* control, $^{***}P < 0.001$, and $^{*}P < 0.05$ *vs* LPS group.

treatment significantly increased the levels of GPX4 and SLC7A11 (Figs. 7C and 7D). Furthermore, AG upregulated the protein and mRNA levels of Nrf2 (Figs. 7E and 7G). and had an impact on its mRNA level (Figs. 7E and 7G). AG counteracted the LPS-induced reduction in Nrf2 and increased the expression of its downstream target genes, *HO-1* and *NQO1* (Figs. 7E and 7G). Additionally, AG reduced the protein and mRNA levels of TLR4 and Keap1 induced by LPS (Figs. 7E and 7G). In conclusion, our findings indicate that AG inhibits ferroptosis in mice by modulating the TLR4/Keap1-Nrf2 signaling pathway, highlighting its potential as a therapeutic agent for managing LPS-induced ALI.

Discussion

Ferroptosis is a unique form of cell death characterized by iron-driven lipid peroxidation, and it is implicated in vari-

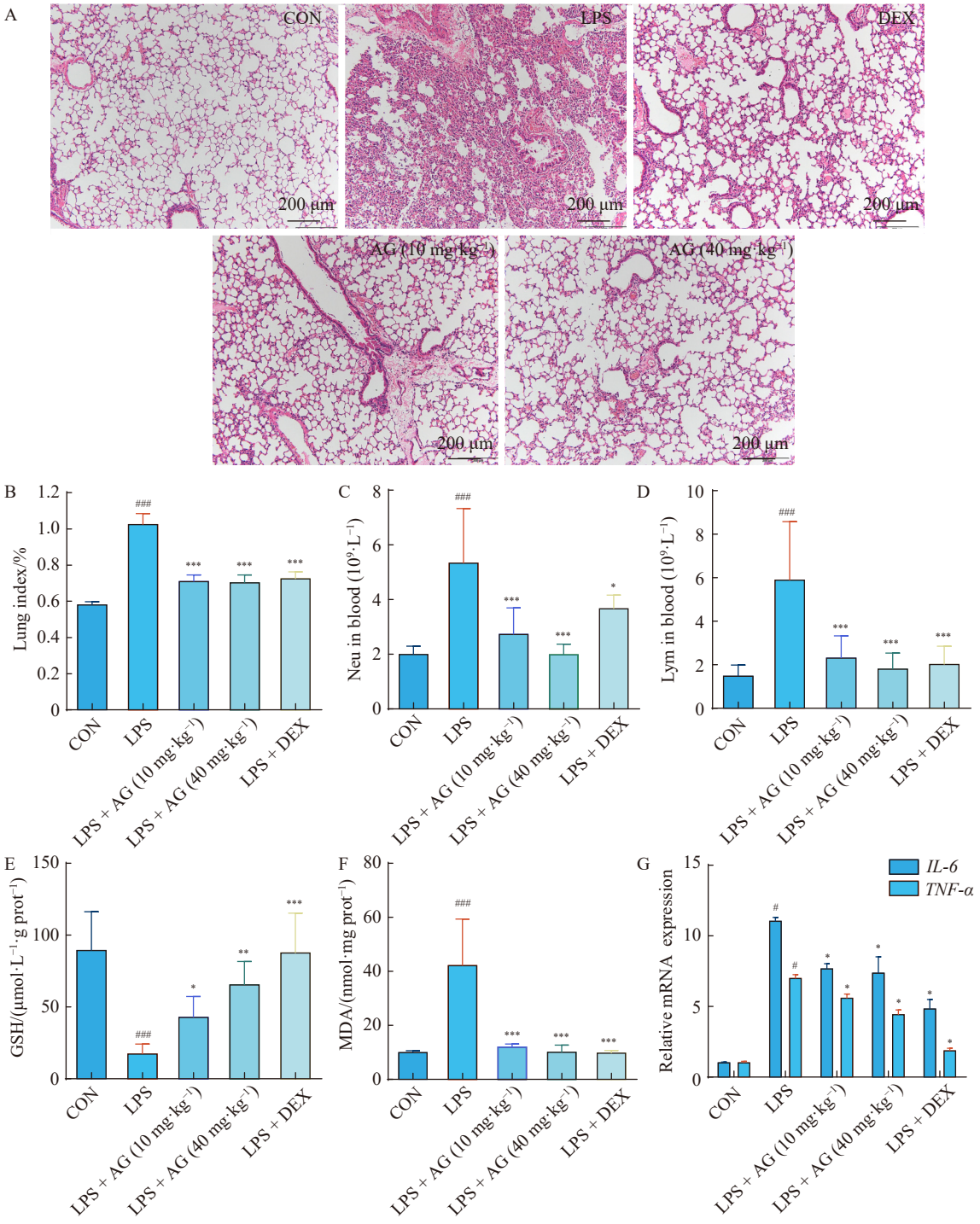

Fig. 6 AG significantly alleviates LPS-induced ALI *in vivo*. (A) Lung histopathology at 24 h after LPS challenge exhibited reduced pulmonary damage in AG-treated mice (scale bar = 100 μm). (B) The lung index, reflecting the severity of ALI. (C) The NEU and Lym counts in the blood were determined using an automated hematology analyzer. The levels of pulmonary MDA (E) and GSH (F) were assessed using the MDA and GSH kits. (G) RT-qPCR was used to assess the mRNA levels of *IL-6* and *TNF-α*. Data were shown as mean ± SD (n = 6). Statistical analysis revealed significant differences: $^{###}P < 0.001$, $^{#}P < 0.05$ *vs* control, $^{***}P < 0.001$, $^{**}P < 0.01$, and $^{*}P < 0.05$ *vs* LPS group.

ous pathological conditions, including neurodegeneration [31], cancer [32], liver diseases [33], and heart diseases [34]. AG, a compound derived from Andrographis paniculata, possesses potent anti-inflammatory properties. AG mitigates inflammation by inhibiting pro-inflammatory cytokines, modulating inflammatory signaling pathways, and suppressing immune cell activation [35]. It is widely used in China and other parts of Asia to treat upper respiratory tract infections due to its

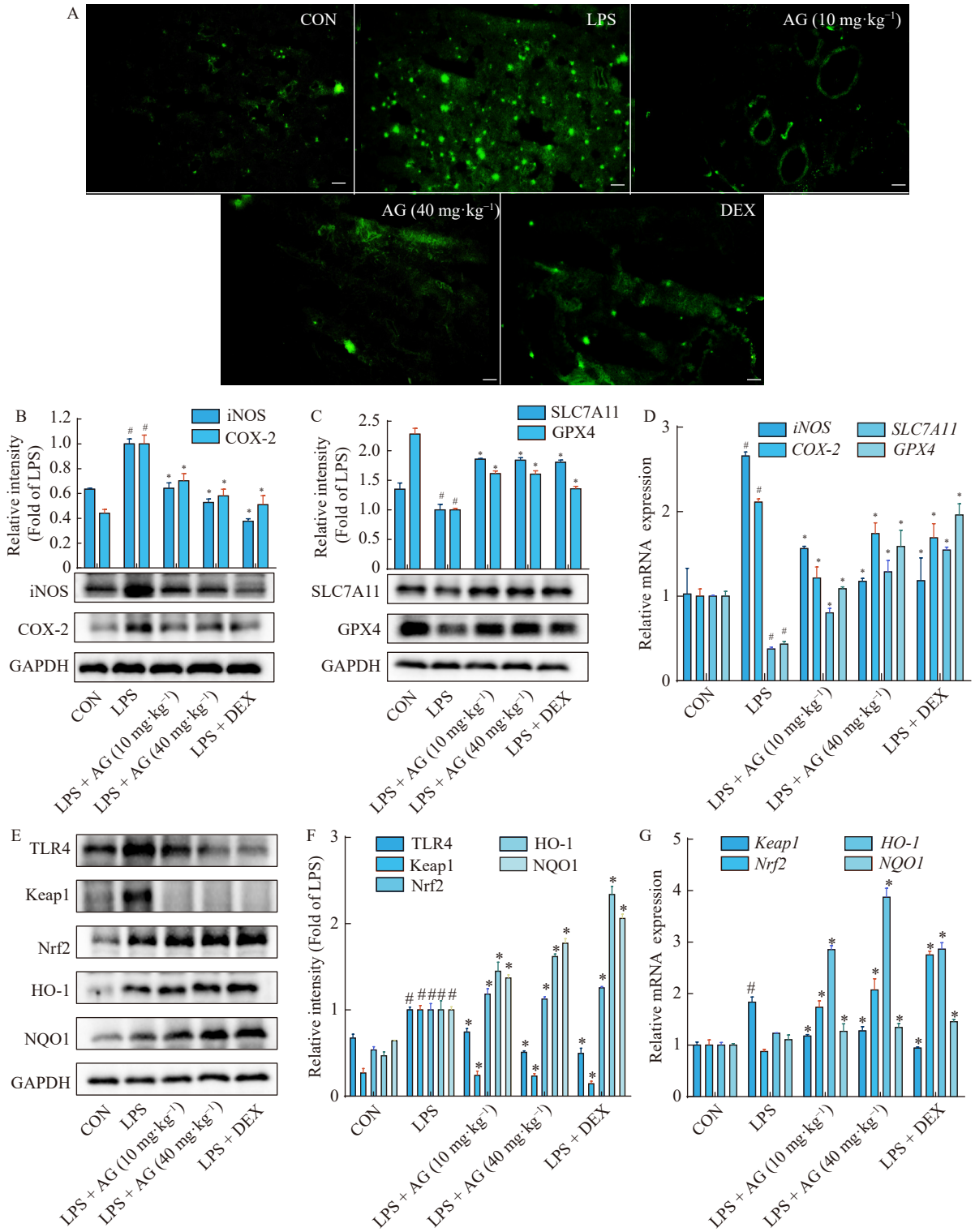

Fig. 7 AG reduced LPS-induced ferroptosis in lung tissue. (A) Representative images of a fluorescence probe for lipid ROS in lung tissue are depicted. (B and C) Western blotting analysis was performed to detect the expression of iNOS and COX-2 in lung tissue. (D) The relative mRNA levels of *iNOS*, *COX-2*, *SLC7A11*, and *GPX4* were determined in lung tissue. (E and F) Western blotting analysis was conducted to examine the levels of toll-TLR4, Keap1, Nrf2, HO-1, and NQO1 in lung tissue. (G) The relative mRNA levels of *Keap1*, *Nrf2*, *HO-1*, and *NQO1* were quantified in murine lung tissue. Data were shown as mean ± SD (n = 6). Statistical analysis revealed significant differences: $^{\#}P < 0.05$ *vs* control group, $^{*}P < 0.05$ *vs* LPS group.

strong anti-inflammatory activity [36]. Previous studies have shown that andrographolide sulfonate ameliorates LPS-induced ALI in mice by down-regulating MAPK and NF-κB pathways [37]. Our research aimed to explore AG's role in

suppressing ferroptosis in ALI, particularly its impact on key elements such as GPX4 and SLC7A11, as well as its antioxidative and anti-ferroptosis capacities. We observed that AG significantly increased both the protein and mRNA levels of GPX4 and SLC7A11, boosted GSH levels, and simultaneously reduced MDA and lipid peroxidation in LPS-activated RAW 264.7 cells (Fig. 2) and ALI models (Figs. 6 and 7). Given that GPX4 and SLC7A11 are crucial in preventing ferroptosis and that GSH acts as a radical-neutralizing antioxidant, the decrease in MDA—a byproduct of lipid peroxidation—highlights AG's antioxidative and anti-ferroptosis capabilities. Furthermore, AG effectively alleviated pulmonary pathological alterations, inflammation, and edema induced by LPS (Fig. 6). These findings enhance our understanding of AG's role in suppressing ferroptosis in LPS-induced ALI, potentially through the alleviation of oxidative stress and regulation of cellular damage, thereby reducing inflammatory responses and pulmonary pathological changes.

TLR4, a cell surface receptor primarily known for detecting bacterial LPS and initiating immune responses [38], also appears to play a crucial role in regulating ferroptosis, a unique form of cell death driven by oxidative stress and lipid peroxidation [39, 40]. Our findings suggest that LPS-induced activation of TLR4 increases intracellular oxidative stress, resulting in lipid peroxidation and decreased cell viability, which are hallmark features of ferroptosis. In this study, we used the TLR4 inhibitor TAK-242 and observed a significant reduction in lipid peroxidation and MDA levels, indicating reduced ferroptosis. TAK-242 also increased the protein and mRNA levels of SLC7A11 and GPX4, as well as GSH levels, all of which are critical in combating oxidative stress and inhibiting ferroptosis. Additionally, TAK-242 improved cell viability after LPS treatment, likely by suppressing TLR4 activation, reducing oxidative stress and lipid peroxidation, and thus inhibiting ferroptosis. These results suggest that TLR4 modulates ferroptosis by promoting oxidative stress and lipid peroxidation (Fig. 4). Conversely, TAK-242 inhibits ferroptosis by blocking TLR4 activation, lowering oxidative stress and lipid peroxidation, and enhancing the levels of SLC7A11, GPX4, and GSH. This provides preliminary evidence of TLR4's role in the regulation of ferroptosis, although further experimental validation is needed. Furthermore, our investigation demonstrated that AG suppresses LPS-induced ferroptosis, potentially through TLR4 inhibition. Our data indicate that AG can reduce LPS-induced TLR4 protein expression. Molecular docking assessments revealed an interaction between AG and the TLR4 protein, which was further corroborated by Biacore (Figs. 5D and 5E) and CETSA-WB experiments (Fig. 5F). These findings highlight the significance of TLR4 in AG-mediated inhibition of LPS-induced ferroptosis.

The TLR4 signaling pathway significantly influences the activation of the Nrf2 pathway [41]. Upon activation, TLR4 triggers the activation of Nrf2, leading to the induction of HO-1 expression. This process involves the generation of ROS and the engagement of downstream signaling molecules [42]. Recent research has revealed that, beyond regulating the antioxidant defense system and maintaining redox homeostasis, Nrf2 also plays a crucial role in governing ferroptosis by controlling downstream target genes essential for oxidative stress balance [43]. Ferroptosis, a unique form of cell death, is characterized by iron-dependent lipid peroxidation. Its regulation involves three critical elements: the availability of phospholipid substrates, the mechanisms driving their peroxidation (such as iron-dependent enzymes and labile iron), and the processes responsible for removing lipid peroxides [44]. Nrf2 is significantly involved in the transcriptional regulation of genes associated with iron metabolism and lipid peroxidation. In addition to GPX4 and SLC7A11, Nrf2 regulates the expression of ferroportin, which is responsible for iron export from cells, and the heavy chain of ferritin (FTH1), which is crucial for cytoplasmic iron storage [45]. An optimal strategy for treating diseases associated with ferroptosis involves pharmacologically modulating the Nrf2 pathway and targeting the upstream regulators of ferroptosis [29]. Previous studies have shown that AG can activate the Nrf2/HO-1 pathway, decreasing ROS levels and inhibiting paraquat (PQ)-induced apoptosis in MLE-12 cells. AG also mitigates oxidative stress and apoptosis in PQ-induced ALI by activating the Nrf2/HO-1 pathway [46]. In this study, we found that AG administration increased the expression of Nrf2 and HO-1 in the lung tissues of mice with ALI and in LPS-induced RAW 264.7 cells. Evaluation of nuclear proteins in RAW 264.7 cells demonstrated that AG treatment reversed the LPS-induced decrease in nuclear Nrf2, suggesting that AG facilitates the nuclear translocation of Nrf2. This, in turn, enhances the transcriptional activity of Nrf2, regulating the expression of downstream markers associated with oxidative stress, such as HO-1 and NQO1. LPS counteracted the inhibitory effects of AG on oxidative stress and ferroptosis. Previous research has indicated that Nrf2 combats iron-induced oxidative stress to impede ferroptosis. Furthermore, suppressing Nrf2 diminishes the protective effects of the ferroptosis inhibitor ferrostatin-1 in lung injury by reducing HO-1 expression [47]. Additionally, Nrf2 activation has been confirmed to prevent erastin-induced ferroptosis [48].

Conclusion

In this study, we provide initial evidence of AG's ability to suppress ferroptosis in a TLR4-regulated Nrf2-dependent manner in LPS-induced ALI. However, it is important to acknowledge the limitations of our study. Our focus primarily centered on establishing the inhibitory effect of AG on ferroptosis by attenuating lipid peroxidation. Nevertheless, further investigation is warranted to elucidate the association between AG and phospholipid substrates, as well as iron metabolism, which requires future exploration.

Supporting Information

Supporting information can be requested by sending E-mail to the corresponding authors.

References

[1] Rudd KE, Johnsonet SC, Agesaal KM, *et al*. Global, regional, and national sepsis incidence and mortality, 1990–2017: analysis for the Global Burden of Disease Study [J]. *Lancet*, 2020, **395**: 200-211.

[2] Sevransky JE, Martin GS, Shanholtz C, *et al*. Mortality in sepsis versus non-sepsis induced acute lung injury [J]. *Crit Care*, 2009, **13**: 1-6.

[3] Yuan R, He J, Huang LT, *et al*. Anemoside B4 protects against acute lung injury by attenuating inflammation through blocking NLRP3 Inflammasome activation and TLR4 dimerization [J]. *J Immunol Res*, 2020, **2020**: 7502301.

[4] He RY, Liu BH, Xiong R, *et al*. Itaconate inhibits ferroptosis of macrophage *via* Nrf2 pathways against sepsis-induced acute lung injury [J]. *Cell Death Discov*, 2022, **8**: 43.

[5] Han S, Yuan R, Cui YS, *et al*. Hederasaponin C alleviates lipopolysaccharide-induced acute lung injury *in vivo* and *in vitro* through the PIP2/NF-κB/NLRP3 signaling pathway [J]. *Front Immunol*, 2022, **13**: 846384.

[6] Yuan Y, Zhai Y, Chen J, *et al*. Kaempferol ameliorates oxygen-glucose deprivation/reoxygenation-induced neuronal ferroptosis by activating Nrf2/SLC7A11/GPX4 axis [J]. *Biomolecules*, 2021, **11**: 923.

[7] Yang SJ, Xie ZP, Zeng Y, *et al*. Salidroside attenuates neuronal ferroptosis by activating the Nrf2/HO1 signaling pathway in Aβ1-42-induced Alzheimer's disease mice and glutamate-injured HT22 cells [J]. *Chin Med (UK)*, 2022, **17**: 1-18.

[8] Bebber CM, Müller F, Clemente LP, *et al*. Ferroptosis in cancer cell biology [J]. *Cancers*, 2020, **12**: 164.

[9] Wu JR, Tuo QZ, Lei P. Ferroptosis, a recent defined form of critical cell death in neurological disorders [J]. *J Mol Neurosci*, 2018, **66**: 197-206.

[10] Li XY, Ma N, Xu JP, *et al*. Targeting ferroptosis: pathological mechanism and treatment of ischemia-reperfusion injury [J]. *Oxid Med Cell Longev*, 2021, **2021**: 1587922.

[11] Liu X, Zhang J, Xie W. The role of ferroptosis in acute lung injury [J]. *Mol Cell Biochem*, 2022, **477**: 1453-1461.

[12] Li N, Wang W, Zhou H, *et al*. Ferritinophagy-mediated ferroptosis is involved in sepsis-induced cardiac injury [J]. *Free Radical Bio Med*, 2020, **160**: 303-318.

[13] Mishima E, Sato E, Ito J, *et al*. Drugs repurposed as antiferroptosis agents suppress organ damage, including AKI, by functioning as lipid peroxyl radical scavengers [J]. *J Am Soc Nephrol*, 2020, **31**: 280-296.

[14] Liu PF, Feng YT, Li HW, *et al*. Ferrostatin-1 alleviates lipopolysaccharide-induced acute lung injury *via* inhibiting ferroptosis [J]. *Cell Mol Biol Lett*, 2020, **25**: 1-14.

[15] Shi K, Xiao YX, Dong Y, *et al*. Protective effects of *Atractylodis lancea* Rhizoma on lipopolysaccharide-induced acute lung injury *via* TLR4/NF-κB and Keap1/Nrf2 signaling pathways *in vitro* and *in vivo* [J]. *Int J Mol Sci*, 2022, **23**: 16134.

[16] He J, Yuan R, Cui XL, *et al*. Anemoside B4 protects against *Klebsiella pneumoniae*- and influenza virus FM1-induced pneumonia *via* the TLR4/Myd88 signaling pathway in mice [J]. *Chin Med (UK)*, 2020, **15**: 1-13.

[17] Lee SS, Katkar GD, Tam JL, *et al*. TLR4 signaling and macrophage inflammatory responses are dampened by GIV/Girdin [J]. *PNAS*, 2020, **117**: 26895-26906.

[18] Han S, Gao HW, Chen SR, *et al*. Procyanidin A1 alleviates inflammatory response induced by LPS through NF-κB, MAPK, and Nrf2/HO-1 pathways in RAW264.7 cells [J]. *Sci Rep (UK)*, 2019, **9**: 15087.

[19] Zhou D, Chang W, Qi J, *et al*. Lung protective effects of dietary malate esters derivatives from *Bletilla striata* against SiO2 nanoparticles through activation of Nrf2 pathway [J]. *Chin Herb Med*, 2023, **15**(1): 76-85.

[20] Li JC, Lu KM, Sun FL, *et al*. Panaxydol attenuates ferroptosis against LPS-induced acute lung injury in mice by Keap1-Nrf2/HO-1 pathway [J]. *J Transl Med*, 2021, **19**: 96.

[21] Talei D, Valdiani A, Maziah M, *et al*. Salt stress-induced protein pattern associated with photosynthetic parameters and andrographolide content in *Andrographis paniculata* Nees [J]. *Biosci Biotech Bioch*, 2015, **79**: 51-58.

[22] Li Y, He SN, Tang JS,*et al*. Andrographolide inhibits inflammatory cytokines secretion in LPS-stimulated RAW264. 7 cells through suppression of NF-κB/MAPK signaling pathway [J]. *Evid-Based Compl Alt*, 2017, **2017**: 8248142.

[23] Varma A, Padh H, Shrivastava N. Andrographolide: a new plant-derived antineoplastic entity on horizon [J]. *Evid-Based Compl Alt*, 2011, **2011**: 815390.

[24] Latif R, Wang CY. Andrographolide as a potent and promising antiviral agent [J]. *Chin J Nat Med*, 2020, **18**(10): 760-769.

[25] Banerjee M, Parai D, Chattopadhyay S, *et al*. Andrographolide: antibacterial activity against common bacteria of human health concern and possible mechanism of action [J]. *Folia Microbiol*, 2017, **62**: 237-244.

[26] Mussard E, Cesaro A, Lespessailles E, *et al*. Andrographolide, a natural antioxidant: an update [J]. *Antioxidants (Basel, Switzerland)*, 2019, **8**(12): 571.

[27] Zhang SB, Hong M, Sun XY. Silybin has therapeutic efficacy against non-small cell lung cancer through targeting of Skp2 [J]. *Acta Mater Med*, 2022, **1**(3):302-313.

[28] Zhao T, Guo X, Sun Y. Iron accumulation and lipid peroxidation in the aging retina: implication of ferroptosis in age-related macular degeneration [J]. *Aging Dis*, 2021, **12**: 529.

[29] Dodson M, Castro-Portuguez R, Zhang DD. NRF2 plays a critical role in mitigating lipid peroxidation and ferroptosis [J]. *Redox Biol*, 2019, **23**: 101107.

[30] Zhu JH, Xiong YX, Zhang YX, *et al*. The molecular mechanisms of regulating oxidative stress-induced ferroptosis and therapeutic strategy in tumors [J]. *Oxid Med Cell Longev*, 2020, **2020**: 1-14.

[31] Ryan SK, Zelic M, Han YN, *et al*. Microglia ferroptosis is regulated by SEC24B and contributes to neurodegeneration [J]. *Nat Neurosci*, 2023, **26**: 12-26.

[32] Mou YH, Wang J, Wu JC, *et al*. Ferroptosis, a new form of cell death: opportunities and challenges in cancer [J]. *J Hematol Oncol*, 2019, **12**: 34.

[33] Chen J, Li X, Ge C, *et al*. The multifaceted role of ferroptosis in liver disease [J]. *Cell Death Differ*, 2022, **29**: 467-480.

[34] Li N, Jiang WY, Wang W, *et al*. Ferroptosis and its emerging roles in cardiovascular diseases [J]. *Pharmacol Res*, 2021, **166**: 105466.

[35] Li XH, Yuan WC, Wu JB, *et al*. Andrographolide, a natural anti-inflammatory agent: an update [J]. *Front Pharmacol*, 2022, **13**: 920435.

[36] Abu-Ghefreh AA, Canatan H, Ezeamuzie CI. *In vitro* and *in vivo* anti-inflammatory effects of andrographolide [J]. *Int Im-*

munopharmacol, 2009, **9**: 313-318.

[37] Peng S, Hang N, Liu W, *et al*. Andrographolide sulfonate ameliorates lipopolysaccharide-induced acute lung injury in mice by down-regulating MAPK and NF-*κ*B pathways [J]. *Acta Pharm Sin B*, 2016, **6**: 205-211.

[38] Gauthier AE, Rotjan RD, Kagan JC. Lipopolysaccharide detection by the innate immune system may be an uncommon defence strategy used in nature [J]. *Open Biol*, 2022, **12**: 220146.

[39] Feng RK, Xiong YF, Lei YR, *et al*. Lysine-specific demethylase 1 aggravated oxidative stress and ferroptosis induced by renal ischemia and reperfusion injury through activation of TLR4/NOX4 pathway in mice [J]. *J Cell Mol Med*, 2022, **26**: 4254-4267.

[40] Zhu KY, Zhu X, Sun SH, *et al*. Inhibition of TLR4 prevents hippocampal hypoxic-ischemic injury by regulating ferroptosis in neonatal rats [J]. *Exp Neurol*, 2021, **345**: 113828.

[41] Zhang LF, Zhang XY, Wang AC, *et al*. Bidirectional crosstalk of the cAMP/ROS-dependent signaling pathways in inflammatory macrophage: an activation of formononetin [J]. *Toxicol Appl Pharm*, 2023, **472**: 116571.

[42] Park C, Cha HJ, Lee H, *et al*. The regulation of the TLR4/NF-*κ*B and Nrf2/HO-1 signaling pathways is involved in the inhibition of lipopolysaccharide-induced inflammation and oxidative reactions by morroniside in RAW 264.7 macrophages [J]. *Arch Biochem Biophys*, 2021, **706**: 108926.

[43] Xiang Q, Zhao YZ, Lin JL, *et al*. The Nrf2 antioxidant defense system in intervertebral disc degeneration: molecular insights [J]. *Exp Mol Med*, 2022, **54**: 1067-1075.

[44] Song XH, Long DX. Nrf2 and ferroptosis: a new research direction for neurodegenerative diseases [J]. *Front Neurosci (Switz)*, 2020, **14**: 267.

[45] Kerins MJ, Ooi A. The roles of NRF2 in modulating cellular iron homeostasis [J]. *Antioxid Redox Sign*, 2018, **29**: 1756-1773.

[46] Zhang DG, Shen FQ, Ma ST, *et al*. Andrographolide alleviates paraquat-induced acute lung injury by activating the Nrf2/HO-1 pathway [J]. *Iran J Basic Med Sci*, 2023, **26**: 653-661.

[47] Kose T, Sharp PA, Latunde-Dada GO. Upregulation of Nrf2 signalling and the inhibition of erastin-induced ferroptosis by ferulic acid in MIN6 cells [J]. *Int J Mol Sci*, 2022, **23**: 15886.

[48] Liu N, Lin XL, Huang CY . Activation of the reverse transsulfuration pathway through NRF2/CBS confers erastin-induced ferroptosis resistance [J]. *Brit J Cancer*, 2020, **122**: 279-292.

Cite this article as: LI Yichen, HUANG Liting, LI Jilang, *et al*. Targeting TLR4 and regulating the Keap1/Nrf2 pathway with andrographolide to suppress inflammation and ferroptosis in LPS-induced acute lung injury [J]. *Chin J Nat Med*, 2024, **22**(10): 914-928.